

Rapid-rate Capability of Micro-/Nano-Structured CoO Anodes with Different Morphologies for Lithium-ion Batteries

Guoyong Huang^{1,2,*}, Shengming Xu^{2,3,*}, Yue Yang², Yongbin Chen^{2,4}, Zongbei, Li²

¹ School of Metallurgy and Environment, Central South University, Changsha 410083, China

² Institute of Nuclear and New Energy Technology, Tsinghua University, Beijing 100084, China

³ Beijing Key Lab of Fine Ceramics, Tsinghua University, Beijing 100084, China

⁴ School of Science, Beijing Jiaotong University, Beijing 100044, China

*E-mail: smxu@tsinghua.edu.cn, hgy@mails.tsinghua.edu.cn

Received: 14 August 2015 / Accepted: 30 September 2015 / Published: 4 November 2015

In this study, special micro-/nano-structured CoO powders with different morphologies (cube, sphere and spindle) have been synthesized successfully. All of micro-scale particles (cube, 1.0-4.0 μm in edge length; sphere, 3.0-7.0 μm in diameter; spindle, 2.0-5.0 μm in length and 1.0-3.0 μm in width) are built up by irregular nano-scale components (10-200 nm) attached to each other. Their specific surface areas are about 4.99 m^2g^{-1} , 5.01 m^2g^{-1} and 15.74 m^2g^{-1} , and their average pore sizes are about 1.89 nm, 1.63 nm and 1.88 nm, respectively. By evaluation with electrochemical measurements, all of them possess high initial discharge capacities (1194.4 mAhg^{-1} , 1208.5 mAhg^{-1} and 1248.7 mAhg^{-1} at 0.8 Ag^{-1}), among which the spindle CoO electrode exhibits the best rapid-rate capability (the discharge capacity retention ratios at 0.8 Ag^{-1} after 50 cycles and at 1.6 Ag^{-1} after 30 cycles are 87.3% and 77.7%).

Keywords: Cobalt oxide, Morphologies, Micro-/nano-structure, Rapid-rate capability, Lithium-ion batteries

1. INTRODUCTION

Recently, various transition metal oxides (*e. g.*, Co_3O_4 [1], CoO [2], NiO [3], MnO [4], CuO [5], TiO_2 [6], SnO [7], *et al.*) and their composites (*e. g.*, CoO/C [8], CoO/carbon nanotubes (CNTs) [9], CoO/graphene [10], CoO/reduced graphene oxides (RGO) [11], Co@CoO [12], CoO@Ti [13], Sn/CoO [14], NiO/CoO/C [15], CoO/ CoFe_2O_4 [16], *et al.*) have been exploited for Li-ion batteries (LIBs) and supercapacitors. Among them, CoO has attracted more attention owing to its excellent Li^+ storage capacities (716 mAhg^{-1}), chemical inertness and fully reversible electrochemical reaction [2,17,18]. However, due to its great initial irreversible capacity loss, large volume change upon charge

and discharge, serious voltage polarization and poor electrical conductivity, its application for storage energy system is limited [9-12].

As we all know, the morphology of electronic material is one of the crucial factors to impact its property [19,20]. For example, ultrathin and highly-ordered CoO nanosheet arrays exhibit excellent cycling capability (1000 mAhg^{-1} after 100 cycles at 1 Ag^{-1}) [21]. Self-assembled mesoporous CoO nanodisks (10 nm in thickness, 3-5 μm in diameter) possess good cycling performance ($\sim 630 \text{ mAhg}^{-1}$ after 400 cycles at 0.8 Ag^{-1}) [22], and CoO/CNTs nanoflowers show high energy density ($\sim 3.5 \text{ mWhcm}^{-3}$ at a current density of 0.25 Acm^{-3}) [9]. Porous CoO/C polyhedron (5-8 μm in length, 4-6 μm in width) retains a reversible capacity of 510 mAhg^{-1} after 50 cycles at 0.1 Ag^{-1} [19]. Therefore, it is meaningful to study the relationship between morphologies of CoO powders and their electrochemical performance. On the other hand, the microstructure of electronic material is another factor to affect its performance. And lots of papers about CoO with nanostructure have been reported. For instance, CoO/RGO nanocomposites deliver a high reversible capacity (960 mAhg^{-1}) after 80 cycles at 0.2 Ag^{-1} [11]. CoO/C nanofiber networks ($\sim 8 \text{ nm}$) exhibit a good discharge capacity (630 mAhg^{-1}) after 50 cycles at 0.1 Ag^{-1} [18]. As a contrast, the manipulation of micro-/nano-structure is an approach recently developed to improve the electronic performance of materials [23]. For example, micro-/nano-structured cubic Co_3O_4 powders (with side length $\sim 2.4 \mu\text{m}$ in average) consisting of nanosheets (30-40 nm in thickness, 20-200 nm in diameter) show excellent capacity retention property at high rates (89.9% after 60 cycles at 1 C) [24]. Spherical micro-/nano-structured Co_3O_4 powders ($\sim 2.0 \mu\text{m}$ in diameter) assembled by nanoparticles ($\sim 100 \text{ nm}$) exhibit superior cycling performance ($\sim 970 \text{ mAhg}^{-1}$ after 140 cycles at 0.4 Ag^{-1} and $\sim 500 \text{ mAhg}^{-1}$ after 500 cycles at 1 Ag^{-1}) [25]. However, very few reports have been published regarding CoO powders with micro-/nano-structures.

Herein, in order to investigate the relationship between the shapes of CoO particles and the electrochemical performance, especially rapid-rate capability, micro-/nano-structured CoO powders with different morphologies were synthesized, and their distinct electrochemical performance as anode materials for LIBs was tested and compared.

2. EXPERIMENTAL SECTION

Preparation of samples. CoO powders with different morphologies: the CoCO_3 precursors with different morphologies (cube, sphere and spindle) have been prepared with the methods mentioned in our previous reports [24,26,27]. The precursors were transferred into a muffle electric furnace, thermal treatment was carried out at $600 \text{ }^\circ\text{C}$ in N_2 for 10 h with a heating ramp of $5 \text{ }^\circ\text{C}\cdot\text{min}^{-1}$. After the reaction was over and the furnace was cooled naturally, black products were collected.

Characterizations. The crystal structure of samples were characterized by X-ray powder diffraction (XRD) (Bruker, D8 Advance) at a scanning rate of $12^\circ\cdot\text{min}^{-1}$ with 2theta range of 20° - 80° . The specific surface area and pore size distribution were tested by the specific surface area and porosity analyzer (Micromeritics, Gemini VII 2390). The micro morphologies were observed by transmission electron microscope (TEM) (JEOL, JSM 2011) and scanning electron microscope (SEM) (ZEISS, MERLIN Compact and JEOL, JSM 5500).

Electrochemical measurements. The electrochemical performance of CoO powders as electrodes was investigated through coin cells, while the lithium metal was used as the reference electrode. The working electrode was prepared by mixing CoO, polytetrafluoroethylene (PTFE) and acetylene black (ATB) with a weight ratio of CoO/ PTFE/ATB = 7:1:2, and the weight of every electrode is about 5 mg. The electrolyte solution prepared by dissolving LiPF₆ (1 mol·L⁻¹) in the mixture of diethyl carbonate (DEC), propylene carbonate (PC) and ethylene carbonate (EC) with a volume ratio of DEC/PC/EC = 1:1:3. The electrode capacity was tested by the battery testing system (Land, CT2001A) with the galvanostatic discharge-charge method at 25 °C. And the cyclic voltammogram (CV) was analyzed in the range of 0.01-3.00 V (vs. Li⁺/Li) at a scan rate of 0.2 mV·s⁻¹ by electrochemical workstation (Princeton, Parstat2273).

3. RESULTS AND DISCUSSION

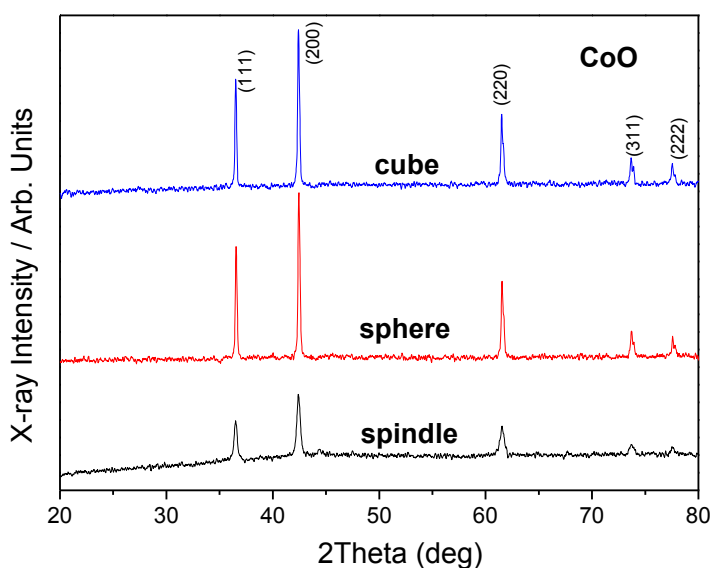


Figure 1. XRD patterns of CoO powders with different morphologies.

Fig. 1 shows the X-ray powder diffraction (XRD) patterns of samples. All of the diffraction peaks match well with the cubic phase CoO (JCPDS no.48-1719), indicating good crystallinity and purity of the CoO powders with different morphologies. The SEM images of CoO samples shown in Fig. 2, it indicates that the morphologies of CoO powders are cubic (Fig. 2a and Fig. 2b), spherical (Fig. 2d and Fig. 2e) and spindle (Fig. 2g and Fig. 2h), respectively. And the edge length of cubic CoO powders ranges between 1.0-4.0 μm, the length of spindles ranges 2.0-5.0 μm and the width ranges 1.0-3.0 μm, and the main diameter of spheres ranges 3.0-7.0 μm. In addition, through the high-magnification SEM images (Fig. 2c, Fig. 2f and Fig. 2i), it can be seen that all samples (cube, sphere and spindle) are built up by irregular nanoparticles with the particle size ranging 10-200 nm attached to

each other. All of them exhibit highly-porous structures among nanoparticles, which are obtained by the heating treatment [28-30].

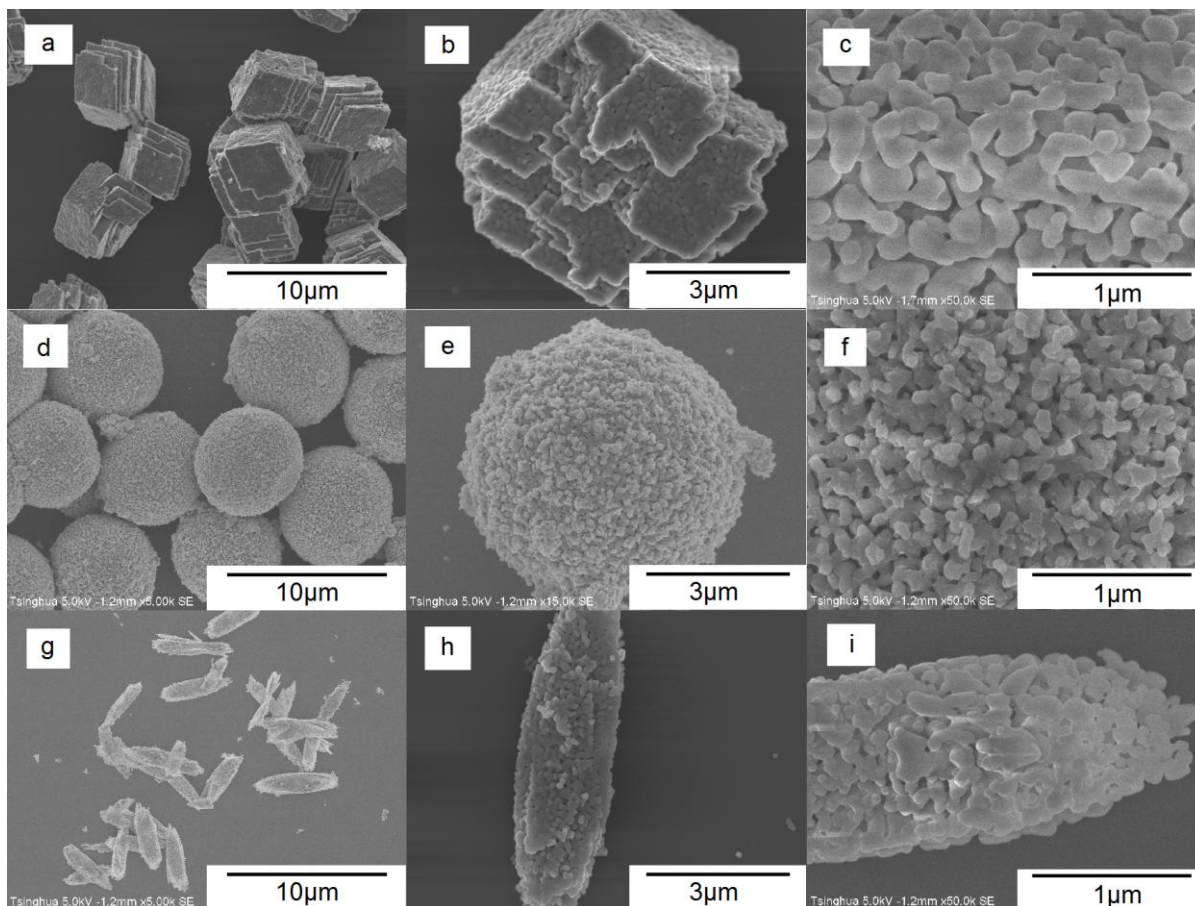


Figure 2. SEM images of CoO powders with different morphologies: (a), (b) and (c) cube; (d), (e) and (f) sphere; (g), (h) and (i) spindle.

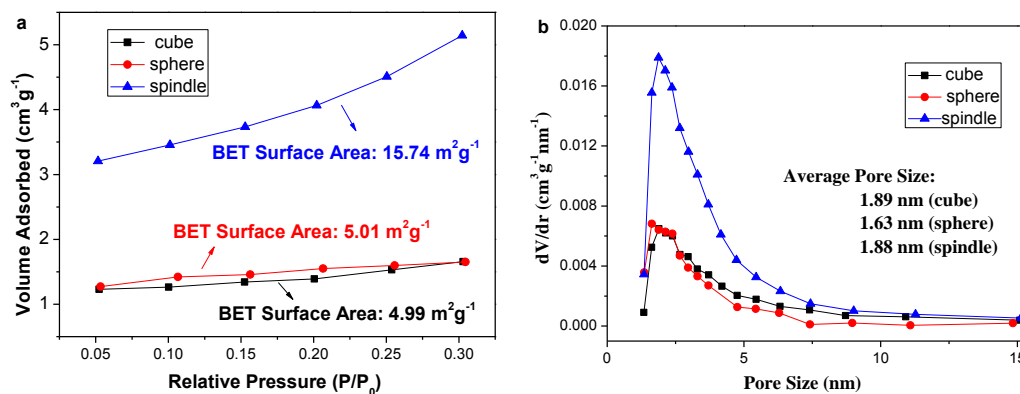


Figure 3. (a) N_2 adsorption isotherms of CoO powders with different morphologies; (b) BJH pore-size distributions of CoO powders with different morphologies.

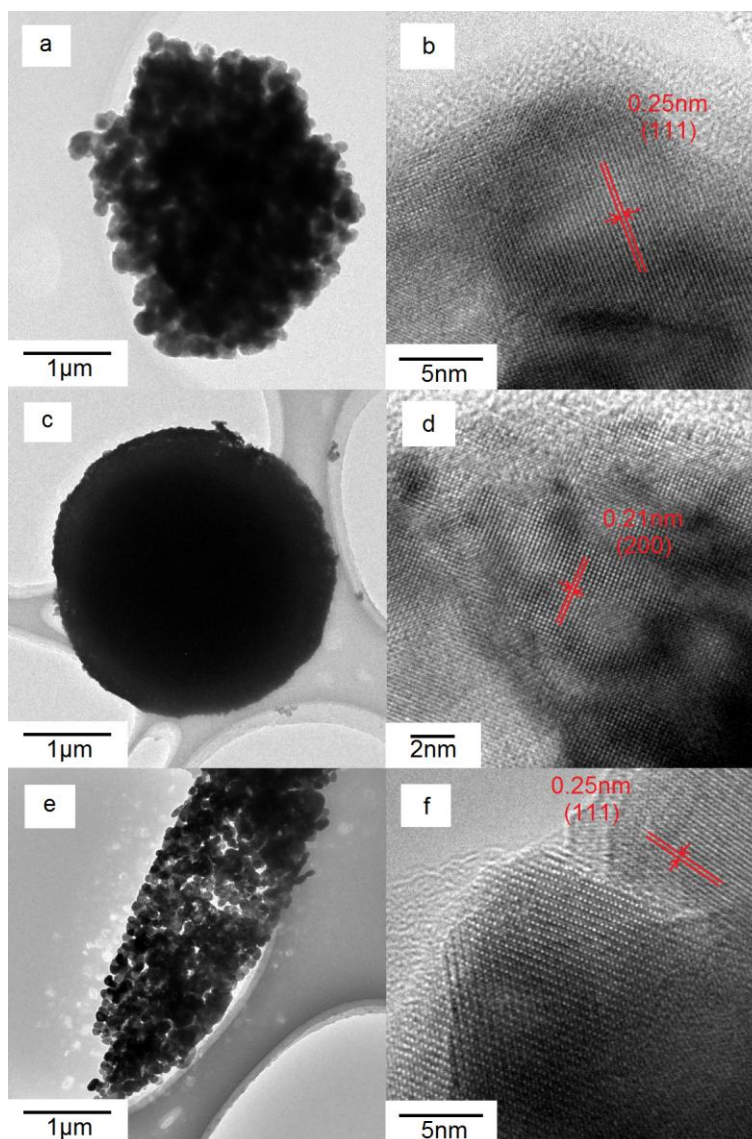


Figure 4. TEM and HRTEM images of CoO powders with different morphologies: (a), and (b) cube; (c) and (d) sphere; (e) and (f) spindle.

Furthermore, the data gained by nitrogen adsorption isotherms (Fig. 3a) show that, the specific surface areas of cubic, spherical and spindle CoO powders are about $4.99 \text{ m}^2\text{g}^{-1}$, $5.01 \text{ m}^2\text{g}^{-1}$ and $15.74 \text{ m}^2\text{g}^{-1}$, respectively. In other words, the surface area of spindle is about three times as the cube's and sphere's. Meanwhile, the data obtained from BJH nitrogen adsorption/desorption isotherms (Fig. S, in Supporting Information) can be used to calculate the pore-size distributions of CoO powders with different morphologies as shown in Fig. 3b. Their average pore sizes are about 1.89 nm, 1.63 nm and 1.88 nm, respectively, and all of them show narrow size distributions (more than 95% in the range of 2.00-5.00 nm). It is further proved by TEM that the morphologies of the corresponding samples are regular cube, sphere and spindle with ultrafine pores (Fig. 4a, Fig. 4c and Fig. 4e). By analyzing the high-resolution transmission electron microscope (HRTEM) images (Fig. 4b, Fig. 4d and Fig. 4f), the lattice fringes of cube and spindle with the spacings of 0.25 nm agree well with the d-spacing of (111)

of cubic phase CoO, while sphere with the lattice spacing of 0.21 nm corresponds to (200) d-spacing, which indicates that some nanoparticles are single-crystal possibly [31,32].

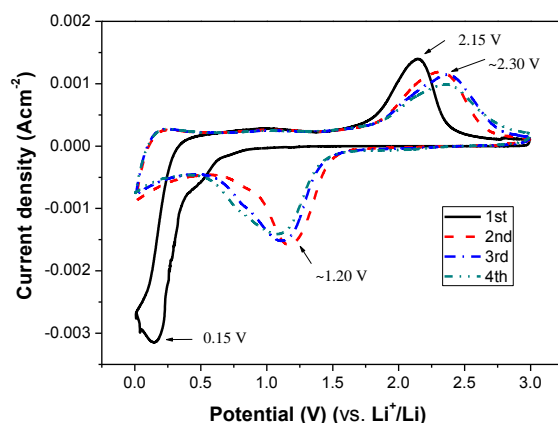
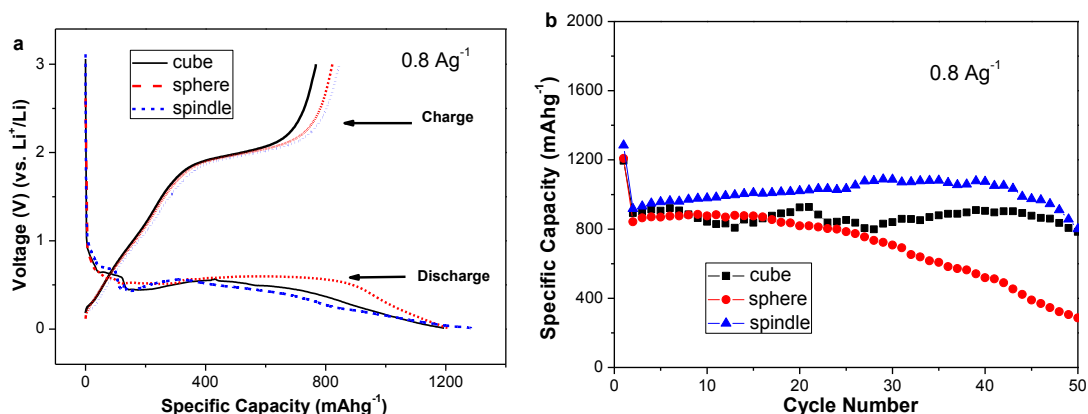
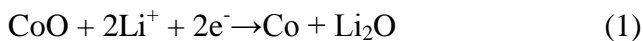


Figure 5. First four cyclic voltammogram curves of cubic CoO electrode at a scan rate of $0.2 \text{ mV}\cdot\text{s}^{-1}$ in the range of 0.01-3.00 V (vs. Li^+/Li).

Since the morphologies of electronic materials affect the CV property little [11,15,19], cubic CoO powders are selected as a representative. The first four CV curves were recorded at a scanning rate of $0.2 \text{ mV}\cdot\text{s}^{-1}$ with the potential range of 0.01-3.00 V (vs. Li^+/Li) (Fig. 5). At the first cycle, an obvious reduction peak is observed at $\sim 0.15 \text{ V}$, which arises from the reduction of CoO to Co [Eqs. (1)]; and a well-defined anodic peak is found at $\sim 2.15 \text{ V}$, which is caused by the oxidation of Co to CoO [Eqs. (2)] [12,22,33]. In the next cycles, all of reduction peaks shift to $\sim 1.20 \text{ V}$, corresponding to the same reduction reaction [Eqs. (1)], while all of oxidation peaks are found at $\sim 2.30 \text{ V}$ with a slight change matching well with the same oxidation reaction [Eqs. (2)]. Therefore, the electrochemical reaction is excellently reversible from the second cycle. Remarkably, due to the formation of irreversible solid electrolyte interface (SEI) film, the intensity of reduction peaks decreases and the value of reduction peak shifts after the initial cycle [12,22,33].



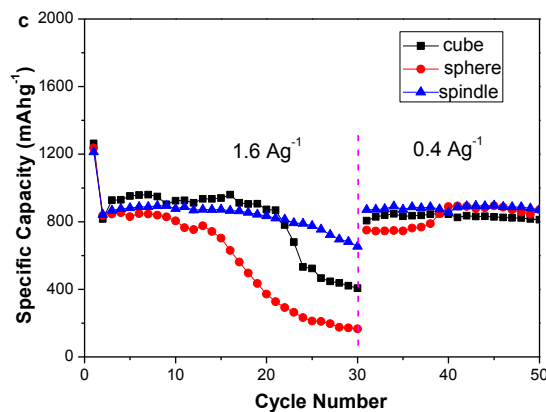


Figure 6. (a) First discharge and charge profiles of CoO electrodes with different morphologies in the range of 0.01-3.00 V (*vs.* Li⁺/Li) at 0.8 Ag⁻¹; Capacity retention properties of CoO electrodes with different morphologies at different current densities: (b) 0.8 Ag⁻¹, (c) 1.6 Ag⁻¹ and 0.4 Ag⁻¹.

The first discharge and charge profiles of CoO electrodes with different morphologies in the voltage range of 0.01-3.00 V (*vs.* Li⁺/Li) at 0.8 Ag⁻¹ are shown in Fig. 6a. All curves share very similar trends. During the discharge, the potential quickly falls to a plateau (0.45-0.60 V) and gradually declines to the cut-off voltage (0.01 V); in the charge curve, the potential slowly goes up to the peak voltage (3.00 V). The first discharge capacities of cube, sphere and spindle are 1194.4 mAhg⁻¹, 1208.5 mAhg⁻¹ and 1248.7 mAhg⁻¹; while the first charge capacities are 767.8 mAhg⁻¹, 822.3 mAhg⁻¹ and 845.9 mAhg⁻¹, respectively. As can be seen, the first irreversible capacity losses are all falling between 32% and 36%, which may be also caused by the formation of irreversible SEI film [23,34]. The cycling performance of CoO electrodes with different morphologies at large current density (0.8 Ag⁻¹) is shown in Fig. 6b. After 50 cycles, the discharge capacity retention ratios of cubic, spherical and spindle CoO electrodes (*versus* the second discharge capacities, *the same below*) are 87.8%, 34.0% and 87.3%, respectively. It indicates that the capacity retention properties of sphere and spindle are both excellent, while that of spherical CoO electrode is not as good. Furthermore, at much larger current density (1.6 Ag⁻¹) shown in Fig. 6c, the discharge capacity of cubic CoO still keeps a high value (~ 870 mAhg⁻¹) after 20 cycles, then slowly falls to a half (~ 406 mAhg⁻¹) at the 30th cycle; the capacity retention ratio of sphere is 84.0% after 15 cycles, then quickly goes down to 19.9% after 30 cycles; meanwhile, the spindle CoO electrode exhibits a high capacity retention ratio (77.7%) after 30 cycles. However, when the current density turns down to 0.4 mAg⁻¹ after 30 cycles, all of capacities can regain to deliver large and stable values (800-880 mAhg⁻¹). Hence, all of micro-/nano-structured CoO anodes with different morphologies possess high initial discharge capacities and enhanced capacity retention property at large current densities; among them, the spindle CoO anode exhibits the best rapid-rate capacity, which performs even better than some composites with CoO [11,16,19]. It can be seen that the property of spindle CoO anode is much better than cube's and sphere's due to much larger specific surface area and more reaction sites in micro-scale [24,26,35]. In addition, because the reversible formation/dissolution of the polymer/gel-like film contributes to an additional reversible capacity, some of CoO capacities as above are higher than its theoretical total capacity (716 mAhg⁻¹) [22,29,30].

The SEM images of the CoO electrodes (mixtures of CoO/ATB/PVDF) with different morphologies after 50 cycles at 0.8 mA g^{-1} are shown in Fig. 7 (cube, Fig.7a; sphere, Fig.7b and spindle, Fig.7c). It indicates that the basic microstructures and shapes have not changed during the charge/discharge, which can be one of reasons for the good cycling performance of these materials.

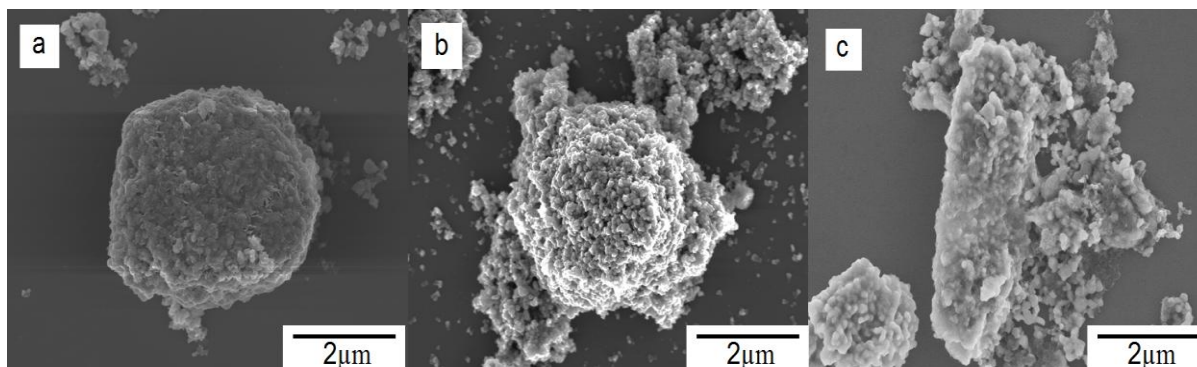


Figure 7. SEM images of CoO electrodes (mixtures of CoO/ATB/PVDF) with different morphologies after 50 cycles at 0.8 A g^{-1} .

4. CONCLUSIONS

In summary, CoO powders with different morphologies (cube, sphere and spindle) have been synthesized successfully, and the electrochemical performance have been evaluated and compared. Because all of them possess the special micro-/nano-structure, which can enhance their electrochemical property obviously, all of the initial discharge capacities are very high ($1194.4 \text{ mAh g}^{-1}$, $1208.5 \text{ mAh g}^{-1}$, and $1248.7 \text{ mAh g}^{-1}$ at 0.8 A g^{-1} , respectively). More remarkable, it is proved that the morphologies of CoO particles may affect the rate capability. Therefore, among them, the spindle CoO electrode, which possesses the most reaction sites and the best electrolyte diffusion, exhibits the best rapid-rate capability (the discharge capacity retention ratios at 0.8 A g^{-1} after 50 cycles and at 1.6 A g^{-1} after 30 cycles are 87.3% and 77.7%).

ACKNOWLEDGMENT

This work was supported by the National Natural Science Foundation of China (Grant Nos. 51274130 and 51074096) and the program for Changjiang Scholars and Innovative Research Team in University (IRT13026).

SUPPORTING INFORMATION

Supporting Information Available: N_2 adsorption/desorption isotherms of CoO powders with different morphologies.

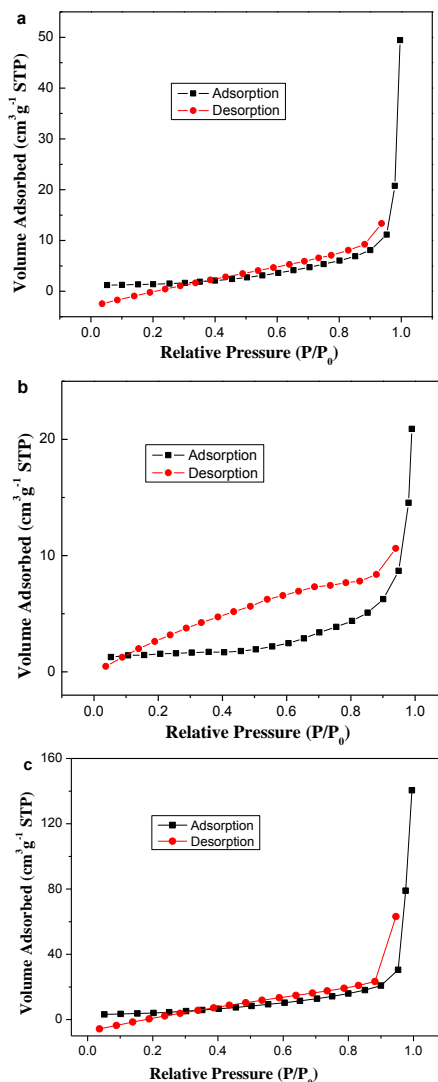


Figure S. N₂ adsorption/desorption isotherms of CoO powders with different morphologies: (a) cube, (b) sphere and (c) spindle.

References

1. H.Y. Sun, Y.G. Liu, Y.L. Yu, M. Ahmad, D. Nan, and J. Zhu, *Electrochim. Acta*, 118 (2014) 1.
2. P. Poizot, S. Laruelle, S. Grugeon, L. Dupont, and J.M. Tarascon, *Nature*, 407 (2000) 496.
3. G.Y. Huang, S.M. Xu, Y.B. Cheng, W.J. Zhang, J. Li, and X.H. Kang, *Int. J. Electrochem. Sci.*, 10 (2015) 2594.
4. S.R. Li, Y. Sun, S.Y. Ge, Y. Qiao, Y.M. Chen, I. Lieberwirth, Y. Yu, and C.H. Chen, *Chem. Eng. J.*, 192 (2012) 226.
5. J.I. Lee, S. Choi, and S. Park, *Chem. Asian J.*, 8 (2013) 1377.
6. A.D.C. Permana, A. Nugroho, K.Y. Chung, W. Chang, and J. Kim, *Chem. Eng. J.*, 241 (2014) 216.
7. Y.J. Hu, K.X. Xu, L.Y. Kong, H. Jiang, L. Zhang, and C.Z. Li, *Chem. Eng. J.*, 242 (2014) 220.
8. H. Qiao, L.F. Xiao, Z. Zheng, H.W. Liu, F.L. Jia, and L.Z. Zhang, *J. Power Sources*, 185 (2008) 486.
9. Y.G. Zhu, Y. Wang, Y. Shi, J.I. Wong, and H.Y. Yang, *Nano Energy*, 3 (2014) 46.
10. W. Deng, W. Lan, Y.R. Sun, Q. Su, and E.Q. Xie, *Appl. Surf. Sci.*, 305 (2014) 433.
11. M. Zhang, Y. Wang, and M.Q. Jia, *Electrochim. Acta*, 129 (2014) 425.

12. L.J. Zhang, P. Hu, X.Y. Zhao, R.L. Tian, R.Q. Zou, and D.G. Xia, *J. Mater. Chem.*, 21 (2011) 18279.
13. J. Jiang, J.P. Liu, R.M. Ding, X.X. Ji, Y.Y. Hu, X. Li, A.Z. Hu, F. Wu, Z.H. Zhu, and X.T. Huang, *J. Phys. Chem. C*, 114 (2010) 929.
14. J. Xu, J. Jin, K. Kim, Y.J. Shin, H.J. Kim, and S.U. Son, *Chem. Commun.*, 49 (2013) 5981.
15. Y.F. Wang, and L.J. Zhang, *J. Power Sources*, 209 (2012) 20.
16. M.X. Li, Y.X. Yin, C.J. Li, F.Z. Zhang, L.J. Wan, S.L. Xu, and D.G. Evans, *Chem. Commun.*, 48 (2012) 410.
17. J.G. Kim, Y. Kim, Y. Noh, and W.B. Kim, *ChemSusChem*, 8 (2015) 1752.
18. X.L. Huang, R.Z. Wang, D. Xu, Z.L. Wang, H.G. Wang, J.J. Xu, Z. Wu, Q.C. Liu, Y. Zhang, and X.B. Zhang, *Adv. Funct. Mater.*, 23 (2013) 4345.
19. W.W. Yuan, J. Zhang, D. Xie, Z.M. Dong, Q.M. Su, and G.H. Du, *Electrochim. Acta*, 108 (2013) 506.
20. G.Y. Huang, S.M. Xu, J.L. Wang, L.Y. Li, and X.J. Wang, *Acta Chim. Sinica*, 71 (2013) 1589.
21. D.D. Li, L.X. Ding, S.Q. Wang, D.D. Cai, and H.H. Wang, *J. Mater. Chem. A*, 2 (2014) 5625.
22. Y.M. Sun, X.L. Hu, W. Luo, and Y.H. Huang, *J. Mater. Chem.*, 22 (2012) 13826.
23. M. Zhang, E. Uchaker, S. Hu, Q.F. Zhang, T.H. Wang, G.Z. Cao, and J.Y. Li, *Nanoscale*, 5 (2013) 12342.
24. G.Y. Huang, S.M. Xu, S.S. Lu, L.Y. Li, and H.Y. Sun, *ACS Appl. Mater. Interfaces*, 6 (2014) 7236.
25. B. Zhang, Y.B. Zhang, Z.Z. Miao, T.X. Wu, Z.D. Zhang, and X.G. Yang, *J. Power Sources*, 248 (2014) 289.
26. G.Y. Huang, S.M. Xu, S.S. Lu, L.Y. Li, and H.Y. Sun, *Electrochim. Acta*, 135 (2014) 420.
27. G.Y. Huang, S.M. Xu, Y. Yang, H.Y. Sun, Z.B. Li, Q. Chen, and S.S. Lu, *Mater. Lett.*, 131 (2014) 236.
28. W. Du, R.M. Liu, Y.W. Jiang, Q.Y. Lu, Y.Z. Fan, and F. Gao, *J. Power Sources*, 227 (2013) 101.
29. H. Guan, X. Wang, H.Q. Li, C.Y. Zhi, T.Y. Zhai, Y. Bando, and D. Golberg, *Chem. Commun.*, 48 (2012) 4878.
30. X.F. Zheng, G.F. Shen, Y. Li, H.N. Duan, X.Y. Yang, S.Z. Huang, H.E. Wang, C. Wang, Z. Deng, and B.L. Su, *J. Mater. Chem. A*, 1 (2013) 1394.
31. M. Zhang, F.L. Yan, X. Tang, Q.H. Li, T.H. Wang, and G.Z. Cao, *J. Mater. Chem. A*, 2 (2014) 5890.
32. Y.M. Sun, X.L. Hu, W. Luo, and Y.H. Huang, *J. Phys. Chem. C*, 116 (2012) 20794.
33. J.C. Liu, Y.Y. Xu, X.J. Ma, J.K. Feng, Y.T. Qian, and S.L. Xiong, *Nano Energy*, 7 (2014) 52.
34. G.Y. Huang, S.M. Xu, L.Y. Li, X.J. Wang, and S.S. Lu, *Acta Phys. -Chim. Sin.*, 30 (2014) 1121.
35. Q. Hao, D.Y. Zhao, H.M. Duan, and C.X. Xu, *ChemSusChem*, 8 (2015) 1435.